Title

Room temperature 3D printing of super-soft and solvent-free elastomers.

Journal

Science advances, 6(46)

ISSN

2375-2548

Authors

Xie, Renxuan
Mukherjee, Sanjoy
Levi, Adam E
et al.

Publication Date

2020-11-13

DOI

10.1126/sciadv.abc6900

Peer reviewed

MATERIALS SCIENCE

Room temperature 3D printing of super-soft and solvent-free elastomers

Renxuan Xie[1,2]*, Sanjoy Mukherjee[1,2]*, Adam E. Levi[3], Veronica G. Reynolds[2,4], Hengbin Wang[2], Michael L. Chabinyc[2,4]†, Christopher M. Bates[1,3,4,5]†

Super-soft elastomers derived from bottlebrush polymers show promise as advanced materials for biomimetic tissue and device applications, but current processing strategies are restricted to simple molding. Here, we introduce a design concept that enables the three-dimensional (3D) printing of super-soft and solvent-free bottlebrush elastomers at room temperature. The key advance is a class of inks comprising statistical bottlebrush polymers that self-assemble into well-ordered body-centered cubic sphere phases. These soft solids undergo sharp and reversible yielding at 20°C in response to shear with a yield stress that can be tuned by manipulating the length scale of microphase separation. The addition of a soluble photocrosslinker allows complete ultraviolet curing after extrusion to form super-soft elastomers with near-perfect recoverable elasticity well beyond the yield strain. These structure–property design rules create exciting opportunities to tailor the performance of 3D-printed elastomers in ways that are not possible with current materials and processes.

INTRODUCTION

Super-soft elastomers are a class of cross-linked materials derived from bottlebrush polymers (*1*, *2*) with substantially smaller shear moduli (ca. 1 to 100 kPa) than traditional rubbers (ca. 1 MPa), even in the absence of solvent (*3*–*5*). The ability to access super-soft mechanical properties without relying on additives that can leach over time is advantageous in a variety of applications ranging from biomimetic tissue (*5*, *6*) to high-sensitivity electronic devices (*7*, *8*). However, a major challenge of using bottlebrush elastomers in these and other contexts lies in processing. Unlike linear elastomers, for which numerous fabrication techniques exist, bottlebrush elastomers are usually formed by simple molding (*4*, *5*, *9*, *10*). Developing super-soft materials that are compatible with more sophisticated processing pathways would create opportunities to leverage their unique mechanical properties in important new directions, e.g., patient-specific implants (*11*) and complex actuator (*12*–*14*) or sensor (*15*) geometries with enhanced performance.

Three-dimensional (3D) printing is a prime example of a versatile processing technique that would expand the application space of bottlebrush elastomers, since it provides exquisite control over the geometry of printed parts beyond what is possible with molding (*16*–*18*). Although 3D printing of uncross-linked bottlebrush polymers has recently been explored for photonic applications (*19*, *20*), to date, there are no examples of 3D-printed bottlebrush elastomers in the literature. In seeking to address this opportunity, we were drawn to a variant of 3D printing known as direct ink writing (DIW), which is operationally simple, widely available, and low cost (*13*, *14*, *16*). DIW involves the extrusion of material from a nozzle that can be dynamically positioned along three coordinate axes (*16*). Because the printed structure must hold its shape, the basis of DIW relies on low-viscosity inks that quickly solidify after deposition. Unfortunately, conventional methods of imparting the requisite ink rheology require nontrivial formulation and engineering optimization that is not ideal for 3D printing bottlebrush elastomers. For example, a common approach involves designing thixotropic mixtures (*21*–*24*) by adding a high concentration of particles (*23*, *24*) that can transmit load by jamming but which yield and slide past one another above a critical stress (*21*, *22*). While widely exploited to extrude conventional silicones with a linear architecture (*18*, *25*), this is not a viable option for printing bottlebrush elastomers, as filler particles would deteriorate the super-soft mechanical properties by increasing stiffness. Alternatively, physical gels swollen with water or organics are known to undergo reversible yielding through transient degradation of the cross-links at low applied stresses (*26*–*28*), but the evaporation of solvent can warp printed parts during DIW or upon drying. Other possibilities include the use of custom instrumentation to control nozzle temperature (*19*) and precisely tuning polymerization kinetics to solidify monomer as it exits the print nozzle (*29*); each of these also increases process complexity and, thus, reduces broad appeal. 3D printing bottlebrush elastomers by DIW, therefore, requires conceptual breakthroughs in ink design.

Here, we tackle this challenge by introducing a general design strategy of bottlebrush inks to 3D-print super-soft elastomers via DIW under ambient conditions in the absence of solvent or thixotropy-inducing additives. Our approach leverages self-assembly to mediate a fast and reversible solid-liquid phase transition at room temperature in response to shear. We elucidate a set of tunable structure-property relationships that reveal the important material parameters affecting facile printability. Formulation with a soluble photocrosslinker enables complete ultraviolet (UV) curing after DIW to form robust, super-soft elastomers. The mechanical performance of these 3D-printed bottlebrush elastomers exhibits two distinct regions of response with near-perfect cyclability (i.e., complete recovery) after being stretched well beyond the yield strain. These conclusions highlight the advantages of exploiting tailored molecular design and self-assembly in contemporary 3D printing processes to generate properties that otherwise cannot be achieved with traditional materials.

[1]Materials Research Laboratory, University of California, Santa Barbara, CA 93106, USA. [2]Mitsubishi Chemical Center for Advanced Materials, University of California, Santa Barbara, CA 93106, USA. [3]Department of Chemistry and Biochemistry, University of California, Santa Barbara, CA 93106, USA. [4]Materials Department, University of California, Santa Barbara, CA 93106, USA. [5]Department of Chemical Engineering, University of California, Santa Barbara, CA 93106, USA.
*These authors contributed equally to this work.
†Corresponding author. Email: mchabinyc@engineering.ucsb.edu (M.L.C.); cbates@ucsb.edu (C.M.B.)

RESULTS

Molecular design and synthesis

With the goal of 3D printing super-soft and solvent-free elastomers at room temperature via DIW, the molecular design of our ink material is motivated by four criteria (Fig. 1). (i) Super-soft mechanical properties. The bottlebrush architecture produces low shear moduli (1 to 50 kPa) as a result of the large volume associated with each entanglement-free network strand (*30*). (ii) Sharp yield-stress behavior. We hypothesized that block copolymer self-assembly could be used to generate thixotropic materials without additives by traversing the order-disorder (solid-liquid) transition (*31*, *32*) in response to shear (*33*–*35*). This type of shear disordering has been reported for the body-centered cubic (BCC) phase of polystyrene-polyisoprene di- and triblock copolymer melts, albeit at high temperatures $T > 100$°C with slow reversibility, inconvenient attributes for DIW. We are unaware of any previous reports describing the use of these or other block copolymers in 3D printing at room temperature without the use of solvent [e.g., water (*28*, *36*) or oil (*27*)], which complicates the printing process and creates potential long-term stability issues. (iii) Fast and reversible yielding at room temperature. Under the assumption that shear disordering and fast reversibility (<100 s) can occur in block copolymer melts well above the glass transition (T_g) and melting (T_m) temperatures of all constituents, we selected short poly(ethylene oxide) (PEO; $T_g = -60$°C, no T_m) and poly(dimethylsiloxane) (PDMS; $T_g = -125$°C, $T_m = -50$°C) as the A and B blocks. Note that both of these materials are biocompatible, which is a potential advantage in many applications of bottlebrush elastomers. Moreover, the large Flory-Huggins interaction parameter between PDMS and PEO ($\chi \approx 0.224$ at 20°C, reference volume = 118 Å^3) (*37*) should improve ordering kinetics by producing a strongly microphase-separated morphology at low degrees of polymerization (N). While both block and statistical sequences of bottlebrush side chains can result in self-assembly (*38*), well-ordered versions of the target BCC phase are notoriously difficult to achieve in the former due to stiffness effects that dilate regions of lamella and cylinder stability (*39*, *40*). Here, we, therefore, opted to explore the self-assembly of statistical PDMS-*stat*-PEO bottlebrushes at extremely asymmetric compositions, a region of phase space that has not been previously studied in detail. (iv) Cross-linkable formulations to generate elastomers after printing. We leverage efficient photocrosslinkers by incorporating small quantities of PDMS bis-benzophenone in the bottlebrush formulation (*7*, *41*), which leaves the shear-thinning behavior essentially unchanged but enables fast curing under UV light (ca. 10 min fully cross-links a 0.4-mm-thick sample at 150 mW/cm^2) to produce super-soft elastomers.

A library of PDMS-*stat*-PEO bottlebrush polymers was synthesized via the grafting-through copolymerization of norbornene-terminated PEO and PDMS macromonomers using ring-opening metathesis polymerization on multigram scale with good control over molar mass dispersity ($Đ < 1.2$) (see the Supplementary Materials for details; table S1 and figs. S1 to S13). For all materials reported herein, the PEO side-chain degree of polymerization was held constant ($N_{SC,PEO} = 10$), while the PDMS length was selected from $N_{SC} = 68$ or 136. As depicted in Fig. 1, the number of PEO (x) and PDMS (y) macromonomer repeat units was varied to produce a total backbone degree of polymerization $N_{BB} = x + y$ with a minority volume fraction of PEO $f_{PEO} = 0.04$ to 0.06. A summary of the characterization data can be found in table S1.

Mesostructure and yield-stress behavior

The proposed yield-stress behavior of PDMS-*stat*-PEO bottlebrush polymers is predicated on their ability to microphase separate into well-ordered spherical domains at room temperature. We therefore first examined the quiescent morphology under ambient conditions. Figure 2A shows synchrotron small-angle x-ray scattering (SAXS) data collected from two samples with different PDMS side-chain lengths, $N_{SC} = 68$ and 136. Both show strong Bragg reflections at $q/q^* = 1:\sqrt{2}:\sqrt{3}:\sqrt{4}$ that are consistent with a well-ordered BCC phase, unexpectedly at extremely asymmetric PEO compositions ($f_{PEO} = 0.04$), which would normally be disordered in a conventional linear block copolymer. Note that the order-disorder transition temperature (T_{ODT}) of these materials can be tuned across a fairly wide range with small changes in f_{PEO} (fig. S14 and table S1), but, in all cases, $T_{ODT} \gg 20$°C ensures robust self-assembly at room temperature. To the best of our knowledge, this is the first evidence that

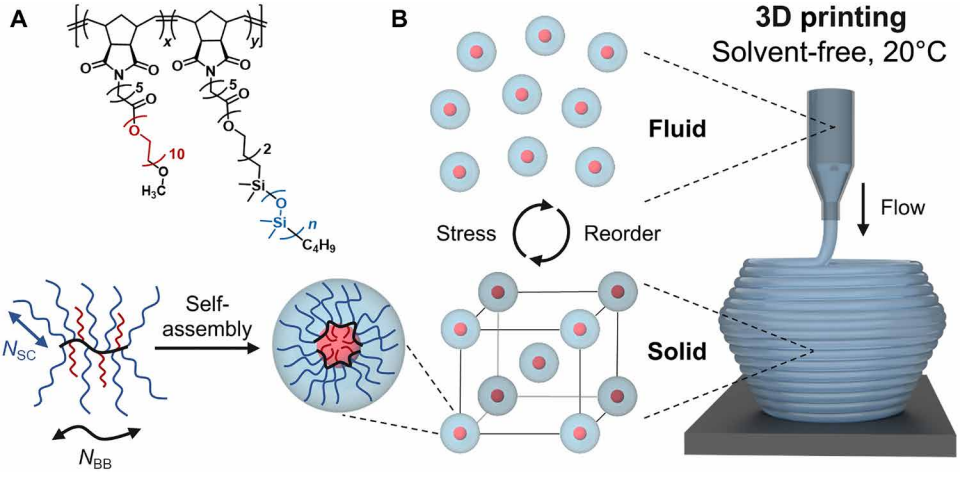

Fig. 1. Bottlebrush polymer design for solvent-free DIW at room temperature. (**A**) Chemical structure and self-assembly of PDMS-*stat*-PEO statistical bottlebrush polymers into BCC spheres at minority PEO volume fractions ($f_{PEO} = 0.04$ to 0.06). (**B**) These soft materials undergo sharp yielding at room temperature in response to shear corresponding with the lattice disordering of PEO micelles, which enables facile extrusion-based 3D printing without solvent or other thixotropy-inducing additives.

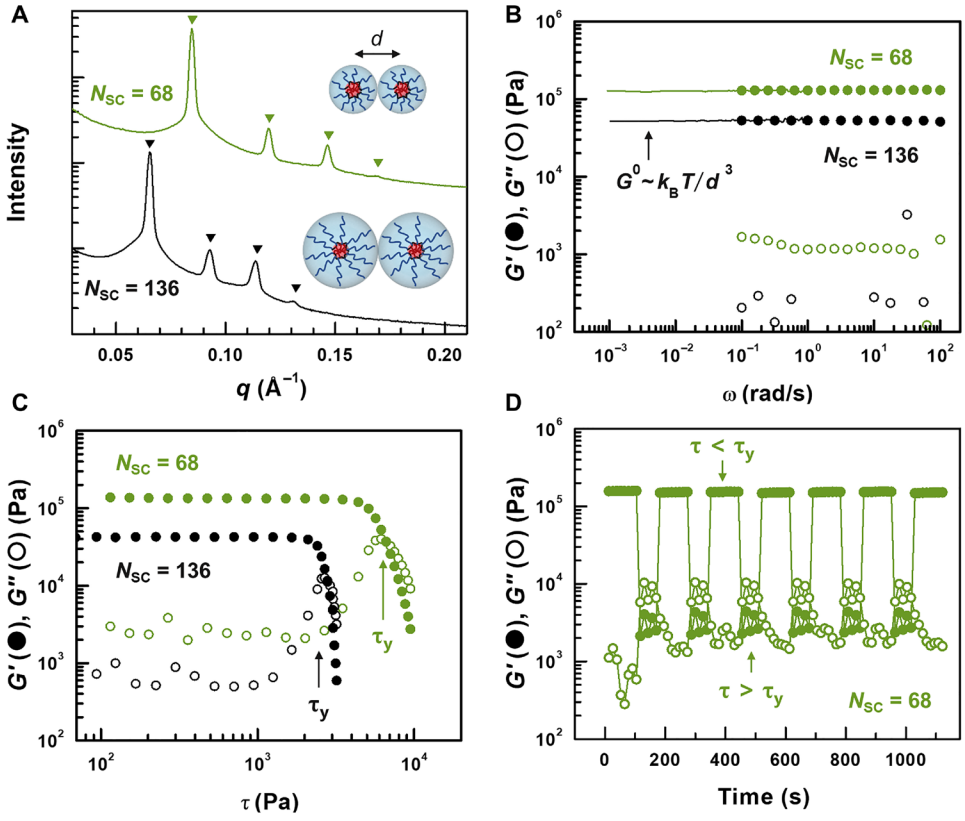

Fig. 2. Morphology and yield-stress behavior of PDMS-*stat*-PEO bottlebrush polymers at 20°C. (**A**) SAXS patterns of samples with N_{SC} = 68 and 136 are consistent with well-ordered BCC unit cells; triangles mark the expected Bragg reflections. The domain spacing (d) depends primarily on N_{SC} (c.f., fig. S15). (**B**) Dynamic frequency sweeps in the linear viscoelastic regime indicate robust, soft solids ($G^0 \approx G' \gg G''$) across five decades in frequency; solid lines are fast Fourier transforms of stress relaxation data (*62*). G^0 depends on d through the as-shown scaling relationship. (**C**) Dynamic stress sweeps (oscillatory frequency = 1.0 rad/s, strain amplitude increases from 0.01 to 1.00) reveal sharp yielding at a critical stress (τ_y) defined as the crossover of G' and G''. The value of τ_y is correlated with N_{SC}, d, and G^0. (**D**) Cyclic dynamic time sweeps between two stresses, 1.4 kPa ($\tau < \tau_y$) and 8.2 kPa ($\tau > \tau_y$), demonstrate reversible yielding, fast reordering kinetics, and excellent mechanical stability. Data were collected at 1.0 rad/s with the sample N_{SC} = 68.

any type of bottlebrush polymer (statistical or blocky) can form high-quality sphere phases (*40*).

We can infer the chain packing in these BCC phases by understanding the dependence of domain spacing ($d^* = 2\pi/q^*$, where q^* is the magnitude of the scattering wave vector at the primary peak) on changes to the backbone (N_{BB}) and PDMS side-chain (N_{SC}) lengths. d^* increases strongly with N_{SC} but is relatively insensitive to N_{BB} and f_{PEO} (fig. S15). These results are consistent with the localization of flexible backbones at the interface between PEO spheres embedded within a PDMS matrix (Fig. 1), as further supported by the close agreement of d^* with a linear analog synthesized using equivalent PEO and PDMS block lengths (fig. S16, A and B). This type of backbone arrangement has been previously identified in statistical bottlebrush melts that form lamellae (*38*, *42*), but we are unaware of any examples involving curved interfaces. The closest analog may be Janus bottlebrushes comprising diblock side chains pinned to the backbone at their junction, which are known to form cylinders and double gyroid networks but have, to the best of our knowledge, yet to be examined in the sphere-forming region of the phase space (*43*, *44*).

The linear viscoelastic response (strain amplitude = 0.01) of PDMS-*stat*-PEO bottlebrush polymers as measured by oscillatory rheology (Fig. 2B) reflects a well-ordered BCC phase at room temperature, where a frequency-independent modulus (G^0) extending across more than five decades in frequency ensures excellent shape retainability over long times. The dependence of G^0 on the nearest-neighbor spacing d between micelles should follow the general scaling relationship for a sphere-forming morphology, $G^0 \sim k_B T/d^3$, where k_B is Boltzmann's constant and T is absolute temperature (*33*). By comparing G^0 in Fig. 2B and d in Fig. 2A for the statistical copolymers with different PDMS side-chain lengths (N_{SC} = 68 and 136), the scaling relationship does hold: $G^0_{N_{SC}=68}/G^0_{N_{SC}=136}$ = 105 kPa/51 kPa = 2.1 is similar to $(d^*_{N_{SC}=136}/d^*_{N_{SC}=68})^3$ = (11.7 nm/9.44 nm)^3 = 1.9. Note that the proportionality constant between d and d^* (hkl = 110) cancels when taking the ratio. In addition, in accordance with the SAXS data, no significant changes in the linear viscoelastic response were observed for samples having identical N_{SC} but different f_{PEO} and N_{BB} (fig. S17). These results conclusively connect the molecular architecture, self-assembled BCC structure, and robust soft-solid characteristics of PDMS-*stat*-PEO statistical bottlebrushes at room temperature.

Sphere-forming PDMS-*stat*-PEO statistical copolymers exhibit sharp yielding at room temperature (Fig. 2C) beyond a critical stress τ_y defined as the crossover of G' and G''. The precise value of τ_y is

tunable through N_{SC}, which is desirable for DIW because the ease of extrusion must be balanced by the mechanical stability of printed features. Figure 2C shows that τ_y is lowered from 6.3 to 2.9 kPa (nearly the same percentage decrease as G^0) by doubling the PDMS side-chain length from N_{SC} = 68 to 136. In addition, similar to the SAXS data and linear viscoelastic response, no significant changes in τ_y were observed for samples with identical N_{SC} but different f_{PEO} and N_{BB} (fig. S18). This implies that the critical yield strain (γ_y) remains constant for statistical bottlebrush copolymers with different N_{SC}, f_{PEO}, and N_{BB}: $\gamma_y = \tau_y/G^0 = 0.11$, as confirmed for both N_{SC} = 68 and 136 by an oscillatory strain sweep (fig. S19A). Our value of γ_y is consistent with Frenkel's prediction (0.10) on the basis of a periodic potential energy between BCC spheres (*33*, *45*) and other types of structured fluids, such as saponite gels (*46*, *47*), but it is somewhat larger than linear diblock copolymer melts (0.038) (*33*). Although the reason for this modest discrepancy is unclear, a larger γ_y with the statistical bottlebrushes may imply fewer BCC lattice defects (*45*) and thus better shape retainability during 3D printing. The solid-liquid phase transition observed with PDMS-*stat*-PEO bottlebrushes is highly reversible and fast at room temperature, occurring within the 12-s data collection step time, as evidenced by experiments that oscillate between two applied stresses, which are smaller and larger than τ_y (Fig. 2D). Additional tests are fully consistent with this behavior, including axial extension (fig. S20A), repeated shear creep recovery (fig. S20B), and cyclic steady shear (i.e., thixotropy loop) (fig. S21). All of these results validate the thixotropic nature of our PDMS-*stat*-PEO bottlebrush copolymers and demonstrate robust mechanical cyclability.

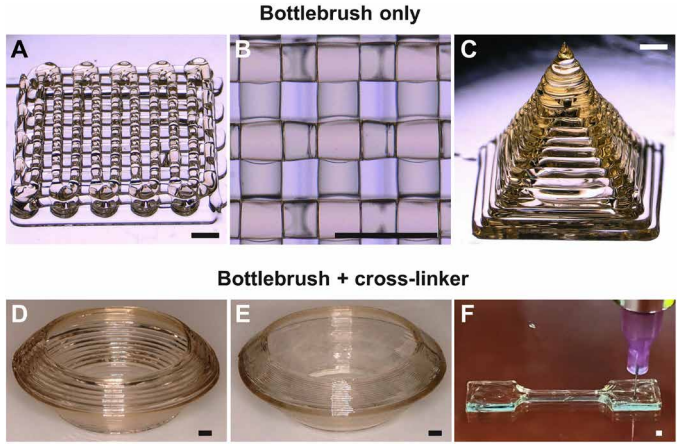

Fig. 3. Room temperature, solvent-free 3D printing of bottlebrush inks. (**A** to **C**) Neat PDMS-*stat*-PEO bottlebrush copolymers (no additives). (A) Log pile (8 mm by 8 mm by 1.5 mm) printed with a 0.80-mm gap and layer thickness of 0.36 mm. (B) Magnified top-down perspective. (C) Hollow pyramid with a layer thickness of 0.36 mm. (**D** to **F**) Formulations of PDMS-*stat*-PEO bottlebrush copolymers that include a photocrosslinker (see Fig. 4 for details). (D) Lower resolution bowl with a layer thickness of 0.28 mm. (E) Higher resolution bowl with a layer thickness of 0.10 mm. Movies are available in the Supplementary Materials. (F) Dog bone with a layer thickness of 0.10 mm. Scale bars, 1 mm. Photo credit: Veronica Reynolds, University of California, Santa Barbara.

3D printing bottlebrush inks

By leveraging the yield-stress behavior of PDMS-*stat*-PEO bottlebrushes, we 3D printed different proof-of-principle objects via DIW after degassing the ink-filled glass syringe in a vacuum oven at 100°C (above T_{ODT}) for 2 hours. When squeezed in the print head at room temperature, self-assembled spheres of PEO mechanically disorder and extrude from the nozzle under low applied pressure. A self-supporting helix formed by the extrudate in movie S1 confirms the immediate recovery of an elastic solid response once stress is removed because of the fast reordering of disordered spheres onto a BCC lattice. This observation suggests that the extrudate can be 3D printed at room temperature in a layer-by-layer fashion with a speed that is limited only by the maximum pressure the stepping motor can apply (see Materials and Methods). Figure 3 (A to C) highlights two different structures printed from the neat PDMS-*stat*-PEO bottlebrushes containing no additives: a four-layer log pile spanning 0.80-mm gaps with a layer thickness of 0.36 mm (Fig 3, A and B), which is typically difficult to achieve without a sharp yield stress and a shear profile that prevents unwanted yielding, and a hollow pyramid with a layer thickness of 0.36 mm (Fig. 3C). Note that both of these printed structures are still soft, yield-stress fluids; only with cross-linking will they be transformed into super-soft elastomers.

Photocrosslinkable formulations

To photocrosslink 3D-printable PDMS-*stat*-PEO bottlebrush copolymers, we designed formulations to include a telechelic PDMS additive ("PDMSbisBP") with benzophenone end groups (Fig. 4A). Benzophenone is well known to react with UV light and generate radicals that can abstract hydrogen atoms from alkyl groups under ambient conditions, which is an efficient method of cross-linking bottlebrush homopolymers (*41*). The choice of benzophenone is also advantageous because its derivatives are well tolerated by the human body and found throughout medicinal chemistry (*48*) and personal care (*49*), suggesting that photocrosslinkers derived therefrom will not compromise the potential biocompatibility of 3D-printed bottlebrush elastomers. To demonstrate that formulations of PDMS-*stat*-PEO and PDMSbisBP can be 3D printed in analogy to the neat bottlebrush copolymers, Fig. 3 (D to F) shows three structures created from a selected PDMS-*stat*-PEO (N_{BB} = 136) mixed with eight PDMSbisBP cross-linkers per bottlebrush molecule (denoted as n_{cl} = 8). We emphasize that this formulation causes little change in the structure (BCC spheres) and rheological response (G^0, τ_y) of the parent PDMS-*stat*-PEO at loadings that are sufficient to form a fully cross-linked elastomer (figs. S22 and S23). Figure 3 (D and E) showcases two bowls that were fabricated with a 45° overhang angle without the need for a support structure (see also movies S2 and S3); the use of different nozzle diameters (0.41 mm, 0.152 mm) provides control over the layer thickness (0.28 mm, 0.10 mm) and print time (40 min, 4 hours). No sag was observed even during the longest prints because of the well-ordered morphology and rheological stability of the photocrosslinkable formulations. We also created a dog bone–shaped specimen with a layer thickness of 0.10 mm (Fig. 3F) to compare the tensile properties of 3D-printed and molded materials (described in more detail below).

Photocrosslinking to form elastomers

Objects fashioned from photocrosslinkable bottlebrush formulations can be readily transformed into elastomers with a high gel fraction (>90%) at room temperature. During the curing process, UV irradiation [365-nm light-emitting diode (LED), 150 mW/cm^2] penetrates the transparent printed part and induces complete cross-linking within 20 min, as evidenced by the plateau of G' and G'' (Fig. 4B and

fig. S24). Although this type of benzophenone-mediated cross-linking is chemically indiscriminate (*41*), the high χ between PDMS and PEO should drive the segregation of PDMSbisBP into the PDMS matrix of the BCC mesophase; we, therefore, expect that the dominant photoreaction will generate intra- and intermolecular bonds between PDMS side chains (illustrated in Fig. 4B) despite a slightly higher propensity for the triplet state of benzophenone to abstract a hydrogen atom from the secondary carbons of PEO (*50*). The development and gradual decrease of phosphorescence intensity originating from the benzophenone triplet states serve as a convenient visual indicator of the transformation from an as-printed yield-stress fluid into a super-soft elastomer (Fig. 4C). The resulting material contains a mix of elastically effective and ineffective cross-links (*41*) with a modulus that is controlled by both the number density of chemical cross-links ($G_x \sim n_{cl}$) and the length scale of microphase separation ($G^0 \sim d^{-3}$) (fig. S25). Irrespective of the N_{SC}, N_{BB}, and f_{PEO} studied here, these UV-cured bottlebrush elastomers are considerably softer (<100 kPa) than traditional, fully cross-linked linear networks (≈1 MPa).

Mechanical properties

To understand the performance of bottlebrush elastomers derived from photocrosslinked PDMS-*stat*-PEO copolymers, we first studied the mechanical properties of samples molded into the shape of a dog bone (i.e., not 3D printed) under uniaxial tension. As shown in Fig. 5A, cyclic loading experiments on cured PDMS-*stat*-PEO bottlebrush elastomers with N_{SC} = 136 and n_{cl} = 8 revealed super-soft mechanical properties and highly unusual recovery after yielding. Two distinct regions of mechanical response are evident, both with quite small shear moduli (G): a linear regime at low extension ratios λ (G_p = 32 kPa) followed by yielding and strain softening at intermediate λ (G_x = 7.7 kPa) [see Supplementary Text and fig. S26 for the calculation of G_p and G_x from tensile data (*5*, *51*)]. Near-perfect recovery was achieved even after applying cyclic deformations well beyond the tensile yield stress (σ_y; horizontal line in Fig. 5A). Each cycle with increasing amplitude exactly reproduces the yielding transition after a rest period of 10 min. The time dependence for elastomer recovery could become important in applications with a high or variable frequency response, but we note that tests performed without pausing between cycles still resulted in excellent recoverability (fig. S27). This highly reversible yielding performance before rupture is uncommon in other materials. For example, particle-filled rubbers cannot completely recover either their shape or pristine mechanical behavior after yielding because of the Mullins effect caused by internal sliding (*52*). Similarly, double network gels and elastomers show full shape recovery but not elasticity beyond the strain-softening point because of irreversible covalent bond degradation in the first network upon large deformation (*53*); the inclusion of ionic cross-links improves recoverable elasticity but still results in permanent set after unloading (*54*).

The unexpected result of recoverability after yielding is evidently related to a reversible structural transition between BCC and disordered micelles that occurs in the cross-linked material when traversing σ_y, as evidenced by in situ SAXS experiments in the

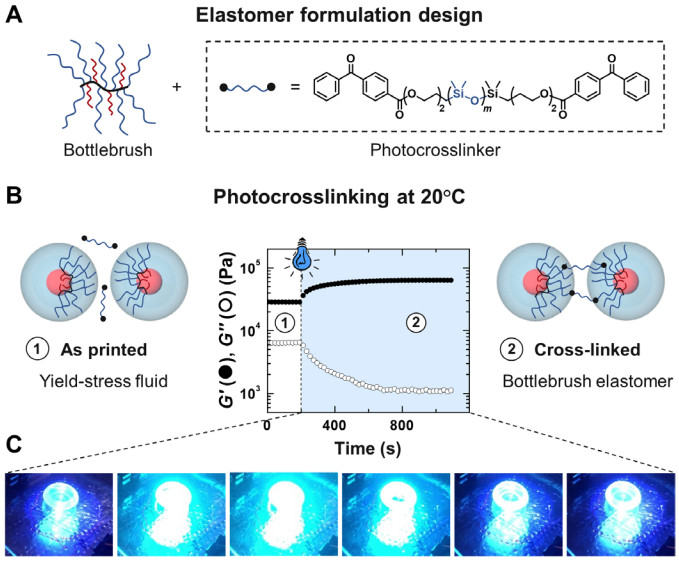

Fig. 4. Photocrosslinking to form super-soft elastomers at room temperature. (**A**) Photocrosslinkable formulations include PDMS-*stat*-PEO bottlebrush copolymers mixed with a bis-benzophenone–based PDMS photocrosslinker. (**B**) UV curing kinetics of PDMS-*stat*-PEO (N_{SC} = 136) with eight cross-linkers per bottlebrush molecule (n_{cl} = 8), as measured by oscillatory rheology (frequency = 1.0 rad/s, strain = 0.01). Sample dimensions: thickness = 0.4 mm, diameter = 20 mm; UV source: irradiance = 150 mW/cm^2, wavelength = 365 nm; see Materials and Methods for details. The illustration highlights the transformation from an as-printed yield stress fluid with discrete micelles to a cross-linked bottlebrush elastomer; note that other possible products of the benzophenone photochemistry (e.g., intramolecular bonds) have been omitted for clarity. (**C**) Photographs capture the development and gradual decrease of phosphorescence intensity, characteristic of benzophenone reactivity, while UV curing the 3D-printed bowl from Fig. 3D. Photo credit: Renxuan Xie, University of California, Santa Barbara.

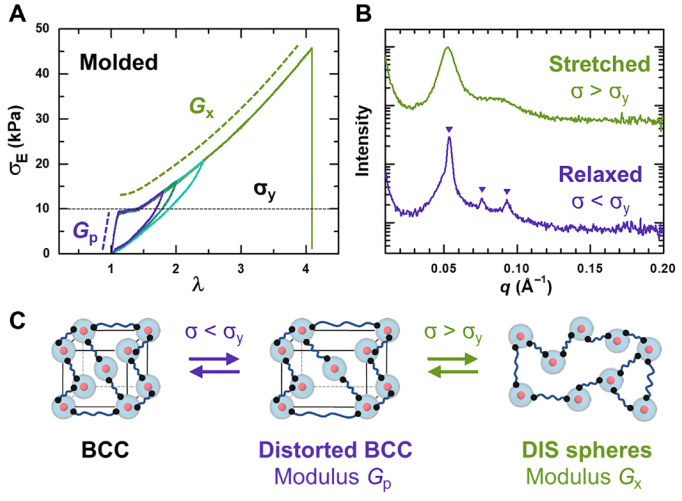

Fig. 5. Structure-property relationships of super-soft elastomers derived from photocrosslinked PDMS-*stat*-PEO bottlebrush copolymers. (**A**) Cyclic uniaxial tensile experiments (engineering stress σ_E versus extension ratio λ) on an elastomer with N_{SC} = 136 and n_{cl} = 8. Note that this sample was processed by molding (see Fig. 6 for 3D printing). Two distinct regions of mechanical response are evident with super-soft shear moduli G_p = 32 kPa and G_x = 7.7 kPa. Near-perfect recovery is possible even after applying strains well above the yield point (σ_y = 10 kPa). Data were collected with 10 min of rest in between cycles and the same 1.0 mm/min loading and unloading rate. (**B**) SAXS experiments demonstrate the unique yielding behavior in the cross-linked elastomeric state is connected to a reversible structural transition between a BCC ($\sigma < \sigma_y$) and lattice-disordered (DIS) ($\sigma > \sigma_y$) arrangement of spheres, as illustrated in (**C**). Triangles mark the expected Bragg reflections of a BCC unit cell.

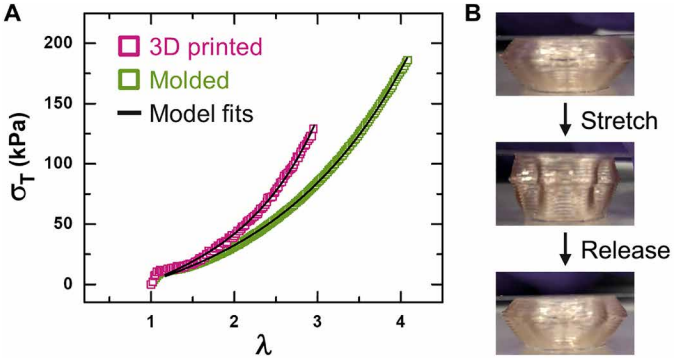

Fig. 6. Mechanical properties of 3D-printed bottlebrush elastomers. (**A**) Uniaxial tensile response of 3D-printed and molded samples (true stress σ_T versus extension ratio λ). Values of the post-yield moduli ($G_{x,molded}$ = 7.7 kPa and $G_{x,printed}$ = 8.6 kPa) were extracted from fits (black lines) to Dobrinyn's model [see Supplementary Text, (*5*, *51*), and table S2]. (**B**) The photocrosslinked, 3D-printed bowl from Fig. 3D is elastic, as evidenced by a series of snapshots taken from movie S4. Photo credit: Renxuan Xie, University of California, Santa Barbara.

relaxed ($\sigma < \sigma_y$) and stretched ($\sigma > \sigma_y$) states (Fig. 5B). Yielding in the elastomeric solid based on a reversible BCC-disordered micelle transformation (Fig. 5C) is analogous to the solid-liquid phase transition observed in noncross-linked PDMS-*stat*-PEO bottlebrushes, which is mediated by an identical mechanism. Further support for this similarity is the quantitative agreement between yield stresses measured in cured (σ_y = 10 kPa; Fig. 5A) and uncured (τ_y = 2.9 kPa; Fig. 2C) samples; the factor of ≈3× difference between tensile and shear stresses is expected for an incompressible material with Poisson's ratio = 0.5. We also note that this morphological behavior is closely related to the structural rearrangements that occur at the order-disorder transition temperature (T_{ODT}) of BCC-forming block copolymers, which formally represents a first-order phase transition involving the lattice disordering of soft micelles (*32*, *55*). For example, shear moduli extracted from tensile experiments in the ordered (G_p = 32 kPa) and disordered (G_x = 7.7 kPa) states as induced by mechanical deformation (Fig. 5A) are consistent with oscillatory rheology measurements in the linear viscoelastic regime at different temperatures: G' = 50 kPa ($T < T_{ODT}$, ordered) and G' = 10 kPa ($T > T_{ODT}$, disordered) (fig. S28). SAXS patterns of the mechanically disordered sample (Fig. 5B) also bear close resemblance to those in a thermally disordered state at $T > T_{ODT}$ (fig. S29).

Next, we compared the mechanical properties of a molded sample (Fig. 5) to the dog bone that was printed in Fig. 3F and subsequently photocrosslinked (Fig. 6). The 3D-printed dogbone was designed with layers oriented parallel to the direction of tensile load, which should probe cohesive failure of the part rather than adhesion between the layers. Although the 3D-printed material is somewhat weaker than the same formulation processed by molding (σ_{max} = 130 versus 185 kPa), it still has a 300% elongation at break and nearly identical yielding behavior. Dobrynin's strain-hardening model (black fit lines in Fig. 6 derived from eq. S3) accurately captures the post-yield response of both the molded and 3D-printed samples, furnishing similar values of $G_{x,molded}$ = 7.7 kPa and $G_{x,printed}$ = 8.6 kPa that are quite soft, as summarized in table S2. We emphasize that these results are only indicative of the mechanical properties in the print direction, and no quantitative testing was done to assess the layer-to-layer strength. Nevertheless, Fig. 6B shows snapshots from movie S4 that qualitatively demonstrate the 3D-printed materials are elastic when subjected to substantial deformation perpendicular to the layers.

DISCUSSION

Relying on self-assembly to produce the requisite BCC phase for efficient shear thinning imposes thermodynamic restrictions on material design and formulation. The details will depend sensitively on polymer sequence and architecture. In the case of statistical bottlebrush copolymers, three degrees of polymerization, $N_{SC,A}$, $N_{SC,B}$, and N_{BB}, must be appropriately selected in addition to the familiar χ and f_A to drive microphase separation at a given cross-linker loading (n_{cl}). Many of these same factors also influence rheological and mechanical properties. The N_{SC} of side chains protruding into the matrix domain controls the yield stress through *d*, the spacing between micelles (Fig. 2). A lower limit on τ_y is therefore determined by the side-chain entanglement molecular weight (maximum N_{SC}) above which kinetic factors would severely hinder efficient DIW. A similar ceiling on N_{BB} is considerably less consequential since bottlebrush backbones only entangle at very large degrees of polymerization (*56*). However, we suspect that N_{BB} cannot be increased ad infinitum without incurring an entropic penalty associated with wrapping long backbones around small spherical cores whose diameter is dictated only by the minority-block side-chain degree of polymerization. Such an effect might destroy the BCC ordering that underpins the utility of these materials as DIW inks. Whether and how these conclusions with the BCC phase translate to other sphere packings, for example, face-centered cubic spheres and tetrahedrally close-packed Frank-Kasper phases (*57*, *58*), remains an open question.

We speculate that the sharp, room temperature shear-thinning behavior of statistical bottlebrush copolymers is a general phenomenon shared by all unentangled block copolymer melts irrespective of chemistry and architecture, subject to constraints involving T_g and micelle connectivity. Rapid and reversible yielding involves the facile rearrangement of self-assembled micelles via lattice disordering and/or defect migration. Intuitively, these mesoscale dynamics are fastest under ambient conditions with rubbery matrix domains that can flow. What about the micelle cores? While here we have focused on soft PEO cores, we anticipate that glassy ones will yield similar results with block sequences and architectures that lack bridging chain configurations. For example, the molecular structure of micelles formed by linear diblocks shares similarities with the statistical bottlebrushes depicted in Fig. 1, where each molecule is confined to a single sphere. We suggest that this chain packing configuration is sufficient to support reversible, room temperature yielding in a BCC phase with either rubbery or glassy micelle cores formed from the minority component. In contrast, ABA triblocks generate sphere phases with a considerable fraction of chains that bridge between micelles; the choice of glassy A blocks ($f_A \ll 0.5$) and rubbery B blocks results in classic thermoplastic elastomers, certainly not yield-stress fluids at room temperature. This versatility of an all-solids ink design, coupled with the diverse array of available cross-linking strategies, should create opportunities to tailor the physical and chemical properties of 3D-printable materials beyond the super-soft elastomers described herein.

In summary, we have demonstrated a new class of direct write inks that enable the 3D printing of super-soft elastomers at room temperature without solvent. A key advance is the design of statistical

bottlebrush copolymers comprising PDMS and PEO side chains that self-assemble into well-ordered BCC spheres at extremely asymmetric compositions (f_{PEO} = 0.04 to 0.06). These materials exhibit fast and reversible yielding at room temperature in response to shear with a yield stress that is easy to manipulate by tuning the PDMS side-chain length. The addition of telechelic PDMS with benzophenone end groups permits simple photocrosslinking after printing to achieve a low-network modulus (<50 kPa) at high gel fractions. Cured elastomers display unusual mechanical performance with near-perfect recoverability well beyond the yield point, which we attribute to the same microphase-mediated lattice-disordering transition that accounts for yielding in uncured samples. This work establishes new paradigms in DIW ink design and highlights the power of novel material development in 3D printing applications.

MATERIALS AND METHODS

Materials

N-(hexanoic acid)-*cis*-5-norbornene-*exo*-dicarboximide was prepared according to literature (*59*). Grubbs' second-generation metathesis catalyst [$(H_2IMes)(PCy_3)(Cl)_2Ru$ = CHPh] was generously provided by Materia. Grubbs' third-generation metathesis catalyst [$(H_2IMes)(pyr)_2(Cl)_2Ru$ = CHPh] (G3) was prepared according to literature (*60*). Methanol (purity of >99.8%; Fisher Scientific, A412), dichloromethane (purity of >99.5%; Fisher Scientific, D37), toluene (purity of >99.5%; Fisher Scientific, T324-500), triethylamine (purity of >99%; Fisher Scientific, ACROS Organics, AC15791), and ethyl vinyl ether (purity of >99%; Fisher Scientific, ACROS Organics, AC119082500) were used as received. $CDCl_3$ (99.8%) was purchased from Cambridge Isotope Laboratories (DLM7) and used as received. Bis(hydroxyalkyl)-terminated PDMS (Sigma-Aldrich, 481246), hydroxyalkyl-terminated PDMS (Gelest, MCR C18 and MCR C22), polyethylene glycol monomethyl ether 550 (TCI, P2184), succinic anhydride (purity of >99%; Sigma-Aldrich, 239690), 4-benzoylbenzoic acid (purity of 99%; Sigma-Aldrich, B12407), *N,N*-dimethylamino pyridine (purity of 99%; Alfa Aesar, H51715), and 1-ethyl-3-(3-dimethylaminopropyl) carbodiimide (purity of 99%; Oakwood Chemical, 024810) were used as received.

Size exclusion chromatography

Size exclusion chromatography was performed on a Waters Alliance HPLC system 2695 separation module equipped with two Agilent PLgel MiniMIX-D bed columns and two detectors: multiangle light scattering (Wyatt DAWN HELEOS-II; 663-nm laser light) and differential refractive index (Wyatt Optilab rEX). The absolute molar mass and molar mass distribution of PEO-*stat*-PDMS bottlebrush polymers were measured in tetrahydrofuran (THF) at 30°C. Polymers were first dissolved in THF overnight with known and dilute concentrations (≤4.0 mg/ml) and then filtered through a 0.45-μm polytetrafluoroethylene filter. The differential refractive index increment (d*n*/d*c*) was calculated by integrating the differential refractive index signal, assuming 100% mass recovery. The number average molar mass (M_n) and molar mass dispersity ($Đ$) were determined by constructing a partial Zimm plot for each slice of the elution profile.

Small-angle x-ray scattering

SAXS data were collected as a function of temperature at the x-ray diffraction facility in the Materials Research Laboratory at the University of California, Santa Barbara (UCSB) using a custom SAXS instrument. PEO-*stat*-PDMS bottlebrush polymers were sealed between Kapton tape inside a metal washer and equilibrated at the set temperature for 10 min before 30 min of x-ray exposure. The hot stage temperature setting was previously calibrated against an external thermometer. In situ SAXS tests under tension were conducted using a stage that holds a stretched (extension ratio $\lambda \approx 1.5$) or relaxed ($\lambda = 1$) dog bone. The instrument included a 50-micron microfocus, Cu target x-ray source (1.54 Å) with a parallel beam multilayer optics and monochromator (Genix from XENOCS SA, France), a high-efficiency scatterless hybrid slits collimator developed in house (*61*), and a PILATUS 100K and EIGER 1M charge-coupled device detector (Dectris, Switzerland). The sample-to-detector distance was 1.7 m. Room temperature SAXS measurements were also performed at the National Synchrotron Light Source II (NSLS-II, beamline 11-BM, Brookhaven National Laboratory) with an x-ray energy of 13.5 keV. For all SAXS experiments, a silver behenate standard was used to calibrate the scattering angles.

Rheological characterization

Rheological characterization of PEO-*stat*-PDMS bottlebrush polymers was performed on a TA Instruments ARES-G2 rheometer in a nitrogen-purged oven. Samples were first preheated above T_{ODT} to adhere to the 25-mm-diameter stainless steel parallel plates before cooling down to 25°C for characterizing the yield-stress fluid behavior. Below the yield stress, the viscoelastic response of PEO-*stat*-PDMS bottlebrush polymers was measured from 100 to 0.1 rad/s with an oscillatory strain amplitude of 0.01, which is well within the linear region. To more quickly probe the long-time (or low frequency) behavior, stress relaxation experiments were performed with a step strain of 0.01, which should be equivalent to that of the oscillatory shear in the linear viscoelastic regime (*30*). Fast Fourier transforming the stress relaxation response from the time to the frequency domain (*62*) resulted in a frequency range that extended from 0.1 to 0.001 rad/s, where the elastic response completely dominates. The order-disorder transition temperature (T_{ODT}) was also probed by linear viscoelastic measurements at a constant frequency of 1.0 rad/s, a strain of 0.01, and a heating rate of 5°C/min.

To probe the yielding transition, multiple types of deformation experiments were performed, including an oscillatory shear amplitude ramp, oscillatory shear time sweeps with cyclic stresses, axial extension, shear creep and recovery with increasing step stresses, and a steady shear thixotropy loop. For oscillatory shear mode, the frequency was held constant at 1.0 rad/s, while the strain amplitude increased from 0.001 to 1 in the amplitude ramp test. In the oscillatory time sweep test, the strain amplitude changed between 0.01 (stress = 1.4 kPa) and 1 (stress = 8.2 kPa) for six consecutive cycles. Data for axial extension tests were collected by raising the top plate at a linear extension rate of 30 μm/s until the sample was completely separated. In transient shear mode, a cyclic creep and recovery test was conducted by increasing the step stress by 25% for each cycle (starting from 2.0 kPa). Each cycle consisted of a creep time of 300 s and recovery time of 100 s. In steady shear mode, a thixotropy loop test was performed by shearing the sample continuously in a clockwise direction and linearly varying the shear rate between 0 and 10 s^{-1}.

In situ UV rheology characterization

In situ UV rheology measurements on a mixture of PEO-*stat*-PDMS bottlebrush polymer and photocrosslinker (PDMSbisBP) were performed with a TA Instruments AR-G2 shear rheometer

equipped with a UV LED accessory (365-nm wavelength; irradiance, 150 mW/cm^2). A 20-mm-diameter parallel plate geometry was used. Photocrosslinkable bottlebrush formulations were cured by exposure to UV light through a 2-cm-thick UV-transparent quartz-bottom plate. An electrically heated top plate was used to control the sample temperature before, during, and after UV curing. Before UV curing, linear oscillatory shear tests were performed to assess the shape retainability of the bottlebrush polymer and photocrosslinker mixture at 25°C with a strain amplitude of 0.01 and a frequency range between 100 and 0.1 rad/s. During UV curing, a constant oscillatory frequency of 1.0 rad/s and strain amplitude of 0.01 were applied to monitor the evolution of shear moduli. After complete curing, as indicated by a plateau in the storage modulus during light exposure, the frequency dependence of the shear moduli between 100 and 0.1 rad/s was collected by linear viscoelastic measurements at 25°C (below T_{ODT}) and at 100°C (above T_{ODT}) with a strain of 0.01.

DIW and UV curing

DIW was achieved by modifying a commercially available 3D printer (LulzBot TAZ Workhorse) with a motor-powered syringe extruder that allows cold extrusion at room temperature. A high-torque stepping motor (MOONS' NEMA 17) was used as the pressure source. After loading the dry mixture of PEO-*stat*-PDMS bottlebrush polymer and photocrosslinker in a glass syringe, the sample was degassed by heating it above its T_{ODT} (at 100°C) in a vacuum oven for 2 hours. Different blunt-dispensing needles (30 gauge, inner diameter = 0.15 mm and 22 gauge, inner diameter = 0.41 mm) with a length of 6.35 mm were used to demonstrate control over 3D printing resolution. At a print speed of 50 mm/min, the apparent shear rate [$\dot{\gamma} = \frac{3.34\,Q}{\pi R^3}$ (*63*), where Q is the volumetric flow rate and R is the inner radius] experienced in the needle tip is estimated to be 37 s^{-1} (30 gauge) and 14 s^{-1} (22 gauge), much larger than the highest shear rate (1.0 s^{-1}) possible in a cone and plate rotational rheometer with no edge fracture. The material response at such a high shear rate can only be extrapolated from the low shear rate response by fitting rheological data with a power-law model (i.e., $\eta = K\dot{\gamma}^{n-1}$, where n = 0.22, and K = 14,000 Pa s^n). On the basis of the expression for the flow of a power-law fluid in a circular channel, $\Delta P = \frac{2KL}{R}\left(\frac{Q\left(3+\frac{1}{n}\right)}{\pi R^3}\right)^n$ (*63*), the minimum pressure drop across a 30-gauge needle tip (length, L = one-quarter inch) is estimated to be 6 MPa.

A bowl-shaped structure with a total height of 6 mm, a maximum diameter of 20 mm, and a wall thickness of 0.6 mm was printed on a glass substrate within either 40 min or 4 hours depending on the choice of needle and corresponding layer thickness (0.28 or 0.10 mm, respectively). The 3D-printed objects were then UV cured under a 365-nm narrow-band UV LED light at an irradiance of 150 mW/cm^2 (Thorlabs SOLIS-365C) for about 20 min until the phosphorescence diminished, which is a signature of the cross-linking reaction involving benzophenone. Using the same composition of bottlebrush polymer and photocrosslinker, a dog bone–shaped sample was also printed with 0.10-mm-thick layers parallel to the tensile direction followed by the same UV curing process. Other structures, including a log pile and hollow pyramid, were printed with a layer thickness of 0.36 mm (22-gauge needle) using only PEO-*stat*-PDMS (i.e., no added cross-linker) to demonstrate its 3D printability. The helical extrudate featured in movie S1 was also formed by dispensing PEO-*stat*-PDMS polymer using a syringe pump (KD Scientific) and a 16-gauge needle (inner diameter = 1.19 mm) oriented horizontally.

Uniaxial tensile tests

Uniaxial tensile testing was performed on 1.0-mm-thick dog bone–shaped specimens (gauge width = 1.5 mm, gauge length = 10 mm) using a custom-built setup with a vertical TwinRail positioning table (Lintech, CA) and a 4.45 N load cell (LSB200 Miniature S-Beam, FUTEK, CA). Dog bone samples were firmly attached to the metal clamps by applying Super Glue for 30 min before testing. During uniaxial tensile tests, the same rate of deformation (1.0 mm/min) was used during loading and unloading. Cyclic loading experiments were held at zero force between cycles by reducing the applied strain as specimens contracted.

SUPPLEMENTARY MATERIALS

Supplementary material for this article is available at http://advances.sciencemag.org/cgi/content/full/6/46/eabc6900/DC1

REFERENCES AND NOTES

1. R. Verduzco, X. Li, S. L. Pesek, G. E. Stein, Structure, function, self-assembly, and applications of bottlebrush copolymers. *Chem. Soc. Rev.* **44**, 2405–2420 (2015).
2. J. Rzayev, Molecular bottlebrushes: New opportunities in nanomaterials fabrication. *ACS Macro Lett.* **1**, 1146–1149 (2012).
3. S. S. Sheiko, A. V. Dobrynin, Architectural code for rubber elasticity: From supersoft to superfirm materials. *Macromolecules* **52**, 7581–7546 (2019).
4. W. F. M. Daniel, J. Burdyńska, M. Vatankhah-Varnoosfaderani, K. Matyjaszewski, J. Paturej, M. Rubinstein, A. V. Dobrynin, S. S. Sheiko, Solvent-free, supersoft and superelastic bottlebrush melts and networks. *Nat. Mater.* **15**, 183–189 (2016).
5. M. Vatankhah-Varnosfaderani, W. F. M. Daniel, M. H. Everhart, A. A. Pandya, H. Liang, K. Matyjaszewski, A. V. Dobrynin, S. S. Sheiko, Mimicking biological stress–strain behaviour with synthetic elastomers. *Nature* **549**, 497–501 (2017).
6. V. Karimkhani, M. Vatankhah-Varnosfaderani, A. N. Keith, E. Dashtimoghadam, B. J. Morgan, M. Jacobs, A. V. Dobrynin, S. S. Sheiko, Tissue-mimetic dielectric actuators: Free-standing, stable, and solvent-free. *ACS Appl. Polym. Mater.* **5**, 1741–1745 (2020).
7. V. Reynolds, S. Mukherjee, R. Xie, A. E. Levi, A. Atassi, T. Uchiyama, H. Wang, M. Chabinyc, C. M. Bates, Super-soft solvent-free bottlebrush elastomers for touch sensing. *Mater. Horiz.* **7**, 181–187 (2019).
8. M. Vatankhah-Varnoosfaderani, W. F. M. Daniel, A. P. Zhushma, Q. Li, B. J. Morgan, K. Matyjaszewski, D. P. Armstrong, R. J. Spontak, A. V. Dobrynin, S. S. Sheiko, Bottlebrush elastomers: A new platform for freestanding electroactuation. *Adv. Mater.* **29**, 1604209 (2017).
9. W. F. M. Daniel, G. Xie, M. Vatankhah Varnoosfaderani, J. Burdyńska, Q. Li, D. Nykypanchuk, O. Gang, K. Matyjaszewski, S. S. Sheiko, Bottlebrush-guided polymer crystallization resulting in supersoft and reversibly moldable physical networks. *Macromolecules* **50**, 2103–2111 (2017).
10. J. L. Self, C. S. Sample, A. E. Levi, K. Li, R. Xie, J. Read de Alaniz, C. M. Bates, Dynamic bottlebrush polymer networks: Self-healing in super-soft materials. *J. Am. Chem. Soc.* **142**, 7567–7573 (2020).
11. M. E. Prendergast, J. A. Burdick, Recent advances in enabling technologies in 3d printing for precision medicine. *Adv. Mater.* , 1902516 (2019).
12. A. Chortos, E. Hajiesmaili, J. Morales, D. R. Clarke, J. A. Lewis, 3D printing of interdigitated dielectric elastomer actuators. *Adv. Funct. Mater.* **30**, 1907375 (2020).
13. A. D. Valentine, T. A. Busbee, J. W. Boley, J. R. Raney, A. Chortos, A. Kotikian, J. D. Berrigan, M. F. Durstock, J. A. Lewis, Hybrid 3D printing of soft electronics. *Adv. Mater.* **29**, 1703817 (2017).
14. A. Kotikian, R. L. Truby, J. W. Boley, T. J. White, J. A. Lewis, 3D printing of liquid crystal elastomeric actuators with spatially programed nematic order. *Adv. Mater.* **30**, 1706164 (2018).
15. A. Frutiger, J. T. Muth, D. M. Vogt, Y. Mengüç, A. Campo, A. D. Valentine, C. J. Walsh, J. A. Lewis, Capacitive soft strain sensors via multicore–shell fiber printing. *Adv. Mater.* **27**, 2440–2446 (2015).
16. J. A. Lewis, Direct ink writing of 3D functional materials. *Adv. Funct. Mater.* **16**, 2193–2204 (2006).
17. B. E. Kelly, I. Bhattacharya, H. Heidari, M. Shusteff, C. M. Spadaccini, H. K. Taylor, Volumetric additive manufacturing via tomographic reconstruction. *Science* **363**, 1075–1079 (2019).
18. E. B. Duoss, T. H. Weisgraber, K. Hearon, C. Zhu, W. Small, T. R. Metz, J. J. Vericella, H. D. Barth, J. D. Kuntz, R. S. Maxwell, C. M. Spadaccini, T. S. Wilson, Three-dimensional printing of elastomeric, cellular architectures with negative stiffness. *Adv. Funct. Mater.* **24**, 4905–4913 (2014).

19. B. M. Boyle, T. A. French, R. M. Pearson, B. G. McCarthy, G. M. Miyake, Structural color for additive manufacturing: 3D-printed photonic crystals from block copolymers. *ACS Nano* **11**, 3052–3058 (2017).
20. B. B. Patel, D. J. Walsh, D. H. Kim, J. Kwok, B. Lee, D. Guironnet, Y. Diao, Tunable structural color of bottlebrush block copolymers through direct-write 3D printing from solution. *Sci. Adv.* **6**, eaaz7202 (2020).
21. D. Bonn, M. M. Denn, L. Berthier, T. Divoux, S. Manneville, Yield stress materials in soft condensed matter. *Rev. Mod. Phys.* **89**, 035005 (2017).
22. A. Z. Nelson, R. H. Ewoldt, Design of yield-stress fluids: A rheology-to-structure inverse problem. *Soft Matter* **13**, 7578–7594 (2017).
23. S. Lee, J. Koo, S.-K. Kang, G. Park, Y. J. Lee, Y.-Y. Chen, S. A. Lim, K.-M. Lee, J. A. Rogers, Metal microparticle – Polymer composites as printable, bio/ecoresorbable conductive inks. *Mater. Today* **21**, 207–215 (2018).
24. Y. Jin, C. Liu, W. Chai, A. Compaan, Y. Huang, Self-supporting nanoclay as internal scaffold material for direct printing of soft hydrogel composite structures in air. *ACS Appl. Mater. Interfaces* **9**, 17456–17465 (2017).
25. S.-Z. Guo, K. Qiu, F. Meng, S. H. Park, M. C. McAlpine, 3D printed stretchable tactile sensors. *Adv. Mater.* **29**, 1701218 (2017).
26. T. H. Fedynyshyn, M. T. Lis, J. A. Lewis, Block copolymer ink formulation for 3D printing and method of making a 3D printed radiofrequency (rf) device (2017), p. 45.
27. C. S. O'Bryan, T. Bhattacharjee, S. Hart, C. P. Kabb, K. D. Schulze, I. Chilakala, B. S. Sumerlin, W. G. Sawyer, T. E. Angelini, Self-assembled micro-organogels for 3D printing silicone structures. *Sci. Adv.* **3**, e1602800 (2017).
28. M. Zhang, A. Vora, W. Han, R. J. Wojtecki, H. Maune, A. B. A. Le, L. E. Thompson, G. M. McClelland, F. Ribet, A. C. Engler, A. Nelson, Dual-responsive hydrogels for direct-write 3D printing. *Macromolecules* **48**, 6482–6488 (2015).
29. C. Leibig, D. Gilbert, *CHROMATIC 3D MATERIALS INC.* (Manufacture of three dimensional objects from thermosets, 2018), p. 76.
30. M. Rubinstein, R. H. Colby, *Polymer physics* (Oxford Univ. Press, 2003).
31. X. Wang, E. E. Dormidontova, T. P. Lodge, The order–disorder transition and the disordered micelle regime for poly(ethylenepropylene-*b*-dimethylsiloxane) spheres. *Macromolecules* **35**, 9687–9697 (2002).
32. J. Wang, Z.-G. Wang, Y. Yang, Nature of disordered micelles in sphere-forming block copolymer melts. *Macromolecules* **38**, 1979–1988 (2005).
33. J. M. Sebastian, C. Lai, W. W. Graessley, R. A. Register, Steady-shear rheology of block copolymer melts and concentrated solutions: Disordering stress in body-centered-cubic systems. *Macromolecules* **35**, 2707–2713 (2002).
34. J. M. Sebastian, C. Lai, W. W. Graessley, R. A. Register, G. R. Marchand, Steady-shear rheology of block copolymer melts: Zero-shear viscosity and shear disordering in body-centered-cubic systems. *Macromolecules* **35**, 2700–2706 (2002).
35. J. M. Sebastian, W. W. Graessley, R. A. Register, Steady-shear rheology of block copolymer melts and concentrated solutions: Defect-mediated flow at low stresses in body-centered-cubic systems. *J. Rheol.* **46**, 863–879 (2002).
36. C. R. Fellin, S. M. Adelmund, D. G. Karis, R. T. Shafranek, R. J. Ono, C. G. Martin, T. G. Johnston, C. A. DeForest, A. Nelson, Tunable temperature- and shear-responsive hydrogels based on poly(alkyl glycidyl ether)s. *Polym. Int.* **68**, 1238–1246 (2019).
37. Y. Luo, B. Kim, D. Montarnal, Z. Mester, C. W. Pester, A. J. McGrath, G. Hill, E. J. Kramer, G. H. Fredrickson, C. J. Hawker, Improved self-assembly of poly(dimethylsiloxane-*b*-ethylene oxide) using a hydrogen-bonding additive. *J. Polym. Sci. Part Polym. Chem.* **54**, 2200–2208 (2016).
38. Y. Xia, B. D. Olsen, J. A. Kornfield, R. H. Grubbs, Efficient synthesis of narrowly dispersed brush copolymers and study of their assemblies: The importance of side chain arrangement. *J. Am. Chem. Soc.* **131**, 18525–18532 (2009).
39. E. B. Zhulina, S. S. Sheiko, A. V. Dobrynin, O. V. Borisov, Microphase segregation in the melts of bottlebrush block copolymers. *Macromolecules* **7**, 2582–2593 (2020).
40. H.-F. Fei, B. M. Yavitt, X. Hu, G. Kopanati, A. Ribbe, J. J. Watkins, Influence of molecular architecture and chain flexibility on the phase map of Polystyrene-*block*-poly(dimethylsiloxane) brush block copolymers. *Macromolecules* **52**, 6449–6457 (2019).
41. S. Mukherjee, R. Xie, V. G. Reynolds, T. Uchiyama, A. E. Levi, E. Valois, H. Wang, M. L. Chabinyc, C. M. Bates, Universal approach to photo-crosslink bottlebrush polymers. *Macromolecules* **53**, 1090–1097 (2020).
42. A. E. Levi, J. Lequieu, J. D. Horne, M. W. Bates, J. M. Ren, K. T. Delaney, G. H. Fredrickson, C. M. Bates, Miktoarm stars via grafting-through copolymerization: Self-assembly and the star-to-bottlebrush transition. *Macromolecules* **52**, 1794–1802 (2019).
43. Z.-H. Guo, A. N. Le, X. Feng, Y. Choo, B. Liu, D. Wang, Z. Wan, Y. Gu, J. Zhao, V. Li, C. O. Osuji, J. A. Johnson, M. Zhong, Janus graft block copolymers: Design of a polymer architecture for independently tuned nanostructures and polymer properties. *Angew. Chem. Int. Ed.* **57**, 8493–8497 (2018).
44. K. Kawamoto, M. Zhong, K. R. Gadelrab, L.-C. Cheng, C. A. Ross, A. Alexander-Katz, J. A. Johnson, Graft-through synthesis and assembly of janus bottlebrush polymers from a-branch-b diblock macromonomers. *J. Am. Chem. Soc.* **138**, 11501–11504 (2016).
45. M. Chandross, N. Argibay, Ultimate Strength of Metals. *Phys. Rev. Lett.* **124**, 125501 (2020).
46. R. H. Colby, Block copolymer dynamics. *Curr. Opin. Colloid Interface Sci.* **1**, 454–465 (1996).
47. H. Hoffmann, A. Rauscher, Aggregating systems with a yield stress value. *Colloid Polym. Sci.* **271**, 390–395 (1993).
48. K. Surana, B. Chaudhary, M. Diwaker, S. Sharma, Benzophenone: A ubiquitous scaffold in medicinal chemistry. *MedChemComm.* **9**, 1803–1817 (2018).
49. S. Kim, K. Choi, Occurrences, toxicities, and ecological risks of benzophenone-3, a common component of organic sunscreen products: A mini-review. *Environ. Int.* **70**, 143–157 (2014).
50. G. Dormán, H. Nakamura, A. Pulsipher, G. D. Prestwich, The life of Pi star: Exploring the exciting and forbidden worlds of the benzophenone photophore. *Chem. Rev.* **116**, 15284–15398 (2016).
51. L. R. G. Treloar, *The Physics Of Rubber Elasticity* (Clarendon Press, ed. 3, 1975).
52. J. Diani, B. Fayolle, P. Gilormini, A review on the Mullins effect. *Eur. Polym. J.* **45**, 601–612 (2009).
53. T. Nakajima, Y. Ozaki, R. Namba, K. Ota, Y. Maida, T. Matsuda, T. Kurokawa, J. P. Gong, Tough double-network gels and elastomers from the nonprestretched first network. *ACS Macro Lett.* **8**, 1407–1412 (2019).
54. J.-Y. Sun, X. Zhao, W. R. K. Illeperuma, O. Chaudhuri, K. H. Oh, D. J. Mooney, J. J. Vlassak, Z. Suo, Highly stretchable and tough hydrogels. *Nature* **489**, 133–136 (2012).
55. E. E. Dormidontova, T. P. Lodge, The order–disorder transition and the disordered micelle regime in sphere-forming block copolymer melts. *Macromolecules* **34**, 9143–9155 (2001).
56. H. Liang, B. J. Morgan, G. Xie, M. R. Martinez, E. B. Zhulina, K. Matyjaszewski, S. S. Sheiko, A. V. Dobrynin, Universality of the entanglement plateau modulus of comb and bottlebrush polymer melts. *Macromolecules* **51**, 10028–10039 (2018).
57. M. W. Bates, J. Lequieu, S. M. Barbon, R. M. Lewis III, K. T. Delaney, A. Anastasaki, C. J. Hawker, G. H. Fredrickson, C. M. Bates, Stability of the A15 phase in diblock copolymer melts. *Proc. Natl. Acad. Sci. U.S.A.* **116**, 13194–13199 (2019).
58. M. W. Bates, S. M. Barbon, A. E. Levi, R. M. Lewis, H. K. Beech, K. M. Vonk, C. Zhang, G. H. Fredrickson, C. J. Hawker, C. M. Bates, Synthesis and self-assembly of AB_n miktoarm star polymers. *ACS Macro Lett.* **9**, 396–403 (2020).
59. C. M. Bates, A. B. Chang, N. Momčilović, S. C. Jones, R. H. Grubbs, ABA triblock brush polymers: Synthesis, self-assembly, conductivity, and rheological properties. *Macromolecules* **48**, 4967–4973 (2015).
60. J. A. Love, J. P. Morgan, T. M. Trnka, R. H. Grubbs, A practical and highly active ruthenium-based catalyst that effects the cross metathesis of acrylonitrile. *Angew. Chem. Int. Ed.* **41**, 4035–4037 (2002).
61. Y. Li, R. Beck, T. Huang, M. C. Choi, M. Divinagracia, Scatterless hybrid metal–single-crystal slit for small-angle X-ray scattering and high-resolution X-ray diffraction. *J. Appl. Cryst.* **41**, 1134–1139 (2008).
62. M. Tassieri, M. Laurati, D. J. Curtis, D. W. Auhl, S. Coppola, A. Scalfati, K. Hawkins, P. R. Williams, J. M. Cooper, i-Rheo: Measuring the materials' linear viscoelastic properties "in a step"! *J. Rheol.* **60**, 649–660 (2016).
63. J. M. Dealy, J. Wang, *Melt Rheology and its Applications in the Plastics Industry* (Springer Netherlands, Dordrecht, 2013), Engineering Materials and Processes.

Acknowledgments: We gratefully acknowledge use of the Innovation Workshop within the California NanoSystems Institute, supported by the University of California, Santa Barbara and the University of California, Office of the President, and thank D. Bothman and D. Magnuson for helpful discussions and technical assistance on modifying the 3D printer. X-ray scattering experiments used resources of the National Synchrotron Light Source II, a U.S. Department of Energy (DOE) Office of Science User Facility operated for the DOE Office of Science by Brookhaven National Laboratory under contract DE-SC0012704. The research reported here made use of shared facilities of the UCSB MRSEC (NSF DMR-1720256), a member of the Materials Research Facilities Network (www.mrfn.org). **Funding:** We gratefully acknowledge partial financial support from the Mitsubishi Chemical Center for Advanced Materials (R.X. and S.M.). This material is based on work partially supported by the U.S. Department of Energy, Office of Basic Energy Sciences, under award number DE-SC0019001 (A.E.L. and C.M.B.). V.G.R. was partially supported by the National Science Foundation Graduate Research Fellowship. **Author contributions:** R.X., S.M., A.E.L., V.G.R., H.W., M.L.C., and C.M.B. designed and analyzed experiments and wrote the manuscript. S.M. and A.E.L. synthesized the compounds and performed chemical analysis and structural

characterization. R.X. and V.G.R. performed structural and rheology characterization, 3D printing, photocrosslinking, and tensile testing. **Competing interests:** R.X., S.M., A.E.L., V.G.R., M.L.C., and C.M.B. are inventors on a patent related to this work filed by the University of California, Santa Barbara (no. US 63/011,454; filed, 17 April 2020). The authors declare that they have no other competing interests. **Data and materials availability:** All data needed to evaluate the conclusions in the paper are present in the paper and/or the Supplementary Materials. Additional data related to this paper may be requested from the authors.

Submitted 7 May 2020
Accepted 23 September 2020
Published 13 November 2020
10.1126/sciadv.abc6900

Citation: R. Xie, S. Mukherjee, A. E. Levi, V. G. Reynolds, H. Wang, M. L. Chabinyc, C. M. Bates, Room temperature 3D printing of super-soft and solvent-free elastomers. *Sci. Adv.* **6**, eabc6900 (2020).